Chinese Chemical Letters 32 (2021) 811–815

Contents lists available at ScienceDirect

Chinese Chemical Letters

journal homepage: www.elsevier.com/locate/cclet

Communication

Enhanced thermoelectric performance of hydrothermally synthesized polycrystalline Te-doped SnSe

Pei Li[a,1], Xin Ai[b,1], Qihao Zhang[c,d,*], Shijia Gu[e], Lianjun Wang[a,f,**], Wan Jiang[a,e]

[a] State Key Laboratory for Modification of Chemical Fibers and Polymer Materials, College of Materials Science and Engineering, Donghua University, Shanghai 201620, China
[b] College of Information Science and Technology, Donghua University, Shanghai 201620, China
[c] State Key Laboratory of High Performance Ceramics and Superfine Microstructure, Shanghai Institute of Ceramics, Chinese Academy of Sciences, Shanghai 200050, China
[d] Center of Materials Science and Optoelectronics Engineering, University of Chinese Academy of Sciences, Beijing 100049, China
[e] Institute of Functional Materials, Donghua University, Shanghai 201620, China
[f] Engineering Research Center of Advanced Glasses Manufacturing Technology, Ministry of Education, Shanghai 201620, China

ARTICLE INFO

Article history:
Received 18 April 2020
Accepted 25 April 2020
Available online 30 April 2020

Keywords:
Polycrystalline SnSe
Hydrothermal synthesis
Thermoelectric
Te doping

ABSTRACT

In this study, large-scale Te-doped polycrystalline SnSe nanopowders were synthesized by a facile hydrothermal approach and the effect of Te doping on the thermoelectric properties of SnSe was fully investigated. It is found that the carrier concentration increases due to the reduction of band gap by alloying with Te, which contributes to significant enhancement of electrical conductivity especially at room temperature. Combined with the moderated Seebeck coefficient, a high power factor of 4.59 $\mu W\,cm^{-1}\,K^{-2}$ is obtained at 773 K. Furthermore, the lattice thermal conductivity is greatly reduced upon Te substitution owing to the atomic point defect scattering. Benefiting from the synergistically optimized both electrical- and thermal-transport properties by Te-doping, thermoelectric performance of polycrystalline SnSe is enhanced in the whole temperature range with a maximum *ZT* of ~0.79 at a relatively low temperature (773 K) for $SnSe_{0.85}Te_{0.15}$. This study provides a low-cost and simple low-temperature method to mass production of SnSe with high thermoelectric performance for practical applications.

Thermoelectric (TE) materials which enable the direct energy conversion between electricity and heat have been the focus of attention due to their prospective applications in waste-heat recovery and portable refrigeration [1,2]. The performance of a thermoelectric material is evaluated by the relation of the Seebeck coefficient (α), electrical conductivity (σ), thermal conductivity (κ) and absolute temperature (T), which is defined as the thermoelectric figure of merit, $ZT = \alpha^2\sigma T/\kappa$ [3]. Obviously, a larger *ZT* value requires a high power factor ($\alpha^2\sigma$) together with a low thermal conductivity. During the past decades, numerous approaches have been employed to improve *ZT* through optimizing electrical transport properties by band engineering [4,5], resonant state doping [6,7], energy filtering effect [8], *etc*., and diminishing thermal conductivity by introducing point defects [9,10], second-phase nanostructures [11,12] and multiscale hierarchical architecturing [13,14]. In particular, the IV—VI semiconductor PbTe exhibits excellent thermoelectric performance at the mid-temperature range (500–850 K) [15–17]. However, its large-scale application is limited by the potential heavy-metal pollution of the toxic Pb. In this regard, efforts devoted to exploring TE materials with nontoxic elements are necessary.

SnSe, which is made of nontoxic and abundant elements, has drawn much attention in recent years due to its excellent thermoelectric properties [18–21]. According to the report [22], SnSe single crystals exhibit a remarkable high *ZT* ~2.6 at 923 K along the crystallographic b-axis owing to their intrinsically ultralow lattice thermal conductivity, which is derived from the strong lattice anharmonicity [23]. Nevertheless, the practical application of SnSe single crystals is prevented by the poor machinability, rigid-controlled crystal growth conditions and high

* Corresponding author at: State Key Laboratory of High Performance Ceramics and Superfine Microstructure, Shanghai Institute of Ceramics, Chinese Academy of Sciences, Shanghai 2000050, China
** Corresponding author at: State Key Laboratory for Modification of Chemical Fibers and Polymer Materials, College of Materials Science and Engineering, Donghua University, Shanghai 201620, China
E-mail addresses: zhangqh@mail.sic.ac.cn (Q. Zhang), wanglj@dhu.edu.cn (L. Wang).
[1] These authors contributed equally to this work.

https://doi.org/10.1016/j.cclet.2020.04.046
1001-8417/

cost of production. Therefore, considerable efforts have been focused on exploring high performance polycrystalline SnSe with better machinability and prospect of scale-up applications [24]. Disappointingly, the reported *ZT* values of polycrystalline SnSe are lower thanthat of single crystal due to the comparatively lower σ and higher κ. For pristine polycrystalline SnSe, the *ZT* values are generally lower than 1.0 at about 750 K [25]. It is thus highly desired to develop polycrystalline bulk materials with higher *ZT*.

For thermoelectric materials, doping has been demonstrated as an effective route to optimize the power factor *via* tuning the carrier concentration [26–28]. Besides, doping can also induce point defects and nanoprecipitates to reduce the lattice thermal conductivity [29]. In Ag-doped p-type SnSe, Chen *et al*. achieved a peak *ZT* of 0.6 at about 750 K due to significantly increased carrier density [30]. Wei *et al*. demonstrated that alkali dopants (Li, Na and K) can enhance the carrier concentration of polycrystalline SnSe and achieved *ZT* of 0.8 for 1% Na- or K-doped SnSe at 800 K [31]. Chen *et al*. fabricated bulk $SnSe_{0.9375}Te_{0.0625}$ by solid-state reaction and studied theoretically the effect of Te doping on SnSe, but the Te content was limited to 0 and 0.0625, and the low electrical conductivity resulted in a low power factor of $\sim$0.7 $\mu W\ cm^{-1}\ K^{-2}$ at 673 K [32].

Moreover, production cost is considered as another major evaluation factor of thermoelectric materials for practical application. Hydrothermal synthesis as a low-cost and simple low-temperature method shows better control of size, structure, and morphology of the products compared with traditional synthesis methods such as melting or mechanical alloying [33]. In this respect, hydrothermal method is effective to fabricate micro/nano-sized products which should possess strong anisotropy. Additionally, the solution-grown products with large surface area would bring about more defects [34], which not only can enhance the phonon scattering, but can also act as electron-acceptors to raise the hole concentrations of SnSe [35].

Herein, we adopt the simple and efficient hydrothermal approach for the synthesis of polycrystalline $SnSe_{1-x}Te_x$ nanopowders, which are sintered by spark plasma sintering (SPS) after annealing treatment. The details of synthesis process and characterization are described in Supporting information. Fig. 1a shows the XRD patterns of as-synthesized $SnSe_{1-x}Te_x$ powders (x = 0, 0.05, 0.1, 0.15 and 0.2). All characteristic peaks are well indexed to the orthorhombic SnSe phase with Pnma space group (PDF#48-1224). No other peaks are present in the patterns, indicating the high phase purity of the crystals. Fig. 1b exhibits the enlarged view of the strongest (111) diffraction peak taken from all samples. It can be seen that the (111) peak gradually shifts towards the lower 2θ angle with the increasing Te content, which suggests the enlarged lattice parameters. This shift is attributed to the larger atomic radius of Te (1.35 Å) than that of Se (1.17 Å) [32]. Based on the results, it can be concluded that Te atom successfully substitutes for Se to form the ternary $SnSe_{1-x}Te_x$ compounds by the facile hydrothermal synthesis and annealing process.

The morphological and structural characteristics of $SnSe_{1-x}Te_x$ powders were investigated by FE-SEM and TEM. As a typical sample, detailed SEM and TEM characterization results of $SnSe_{0.85}Te_{0.15}$ powders are presented. SEM images given in Figs. 1c and d clearly show the flower-like feature of as-prepared $SnSe_{0.85}Te_{0.15}$ powders consisting of nanoplates with the thickness of about 200 nm and the width ranging from a few hundred nanometers to several microns, and the $SnSe_{0.85}Te_{0.15}$ powders tend to stack together irregularly. Fig. 1e is the low-magnification TEM micrograph of the $SnSe_{0.85}Te_{0.15}$ powders, in which clear lamellar structure is observed. High-resolution TEM image (Fig. 1f) of $SnSe_{0.85}Te_{0.15}$ shows clear lattice fringes and the labeled lattice spacing of about 2.410 Å and 2.875 Å correspond to the (401) and (400) lattice planes of orthorhombic SnSe, respectively. All these characterizations demonstrate that $SnSe_{0.85}Te_{0.15}$ nanopowders have been successfully synthesized by our facile hydrothermal method.

To investigate the thermoelectric performance of the hydrothermal synthesized $SnSe_{1-x}Te_x$, the annealed powders were sintered into pellets *via* SPS. Figs. 2a and b display the XRD profiles of $SnSe_{1-x}Te_x$ bulk samples taken in the plane perpendicular and parallel to the pressing direction. All diffraction peaks can be well matched to the crystal structure of SnSe and no impurity peaks are present in the patterns. Moreover, it can be found that the diffraction intensity shows an obviously difference in the two different direction. Typically, the strongest diffraction peak changes from (400) crystal plane in the perpendicular direction to (111) crystal planein theparallel direction, suggesting anisotropy features of the $SnSe_{1-x}Te_x$ bulk samples. Figs. 2c and d are typical SEM images on the fractured surface of $SnSe_{0.85}Te_{0.15}$ bulk samples, which reveals the microstructure in the planes perpendicular and parallel to the press direction. The layered morphology along the

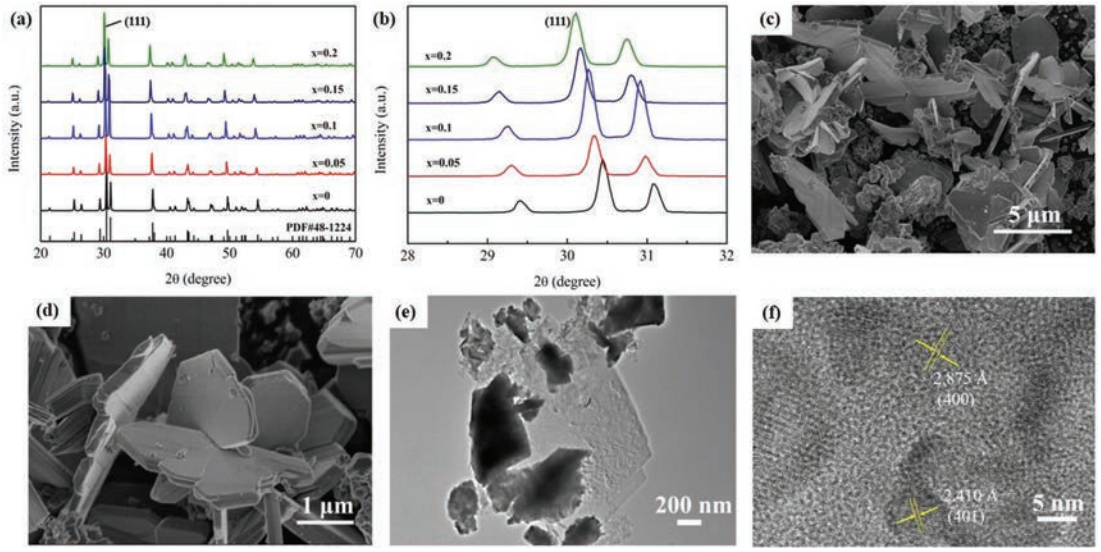

Fig. 1. (a) XRD patterns of $SnSe_{1-x}Te_x$ (x = 0, 0.05, 0.1, 0.15, 0.2) powders and (b) enlarged view of the (111) diffraction peaks. (c, d) SEM images of $SnSe_{0.85}Te_{0.15}$ powder. (e) Low-magnification and (f) high-resolution TEM images of $SnSe_{0.85}Te_{0.15}$ nanopowder.

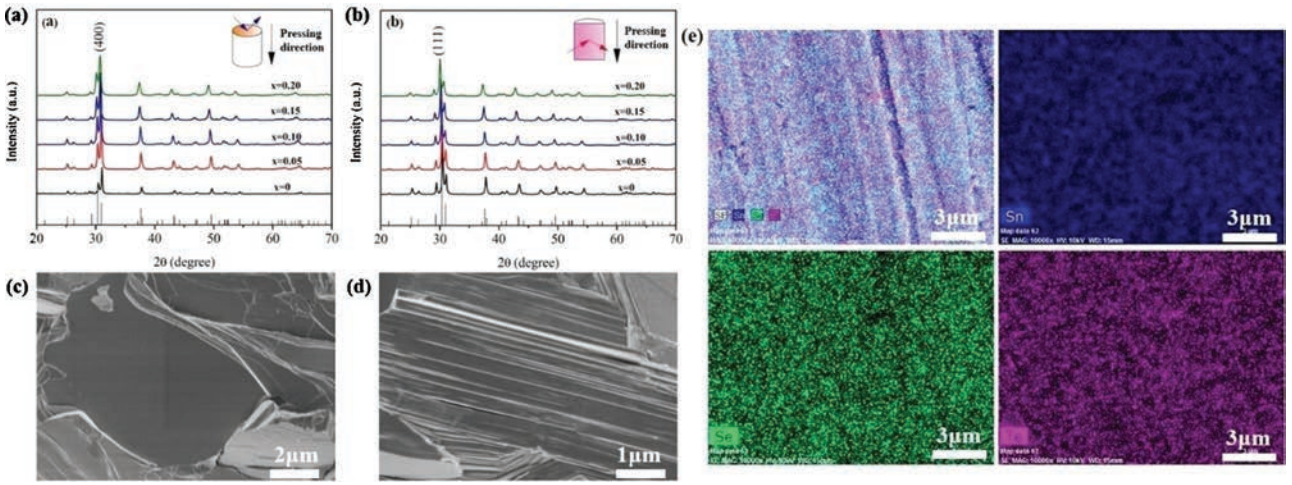

Fig. 2. XRD patterns of bulk $SnSe_{1-x}Te_x$ taken in the plane (a) perpendicular and (b) parallel to the pressing direction. SEM images of the fractured surfaces (c) perpendicular and (d) parallel to the pressing direction. (e) EDS elemental mapping results of all elements, Sn, Se and Te of bulk $SnSe_{0.85}Te_{0.15}$.

parallel direction clearly reveals the preferential orientation of the grains, indicating the strong anisotropic crystal growth. Meanwhile, no obvious micro-cracks or pores can be observed, which is consistent with the high relative density of above 98% as listed in Table 1. Furthermore, the chemical composition and elemental distribution were examined by SEM-EDS and the results of $SnSe_{0.85}Te_{0.15}$ sample are presented in Fig. 2e as a typical example. The results indicate that all elements (Sn, Se and Te) are uniformly distributed without enrichment, which further demonstrates that Te is successfully doped into the SnSe lattice.

The temperature dependence of thermoelectric properties of $SnSe_{1-x}Te_x$ bulk samples were measured along the direction perpendicular to the pressure during SPS process, which present a better thermoelectric transport performance than those measured parallel to the pressure direction in our work. Fig. 3a depicts electrical conductivity σ as a function of temperature for different $SnSe_{1-x}Te_x$ samples. For pristine SnSe, σ firstly increases with increasing temperature, then turns to decrease at ~450 K but finally increases above 650 K. This trend is also found in previous reports, which can be ascribed to amixed scattering mechanism of carrier transport by acoustic phonon and grain boundary potential barrier [36,37]. Compared to pure SnSe, the electrical conductivities of Te-doped samples have been greatly enhanced, especially around room temperature. The maximum electrical conductivity of 98.4 S/cm for the sample $SnSe_{0.8}Te_{0.2}$ is obtained at 300 K. This value is significantly higher than those reported in other polycrystalline SnSe [25,38,39].

Generally, the electrical conductivity is determined by the carrier concentration n and carrier mobility μ according to the equation $\sigma = en\mu$, where e is electron charge. The room-temperature n and μ of $SnSe_{1-x}Te_x$ samples from Hall measurements are presented in Fig. 3b. As can be seen, n is greatly enhanced to the order of 10^{19} cm^{-3} by doping Te and increases with increasing the Te content. The enhancement of n is thought to be caused by the reason that alloying with Te can shrink the width of the band gap [40–42]. This is confirmed by the optical absorption spectra and band gap as shown in Fig. 3c. It shows that the addition of Te changes the shape of the experimental spectra and results in a red-shift of the absorption. As shown in the inset, E_g of pure SnSe in this work is ~0.85 eV, which is well consistent with the reported values [40–42]. E_g keeps decreasing to ~0.65 eV with the increasing Te content, which is responsible for the increase of n with the Te content. At the same time, it can be observed from Fig. 3b that the μ also increased considerably by the introduction of Te. Hydrothermally-synthesized nanopowders tend to have high chemical reactivity due to the fine grains, which could lead to chemisorption of oxygen or generation of crystal defects, resulting in increased trapping of carriers at grain boundaries. The generated energy barriers could impede the motion of carriers from one grain to another [40]. For the Te-doped samples with a larger carrier density, the chemical potential is deeper in the valence band, which means that hole carriers have a higher average energy to get rid of the trap of defects at grain boundaries, thus showing a lower barrier height and a higher mobility [40]. Therefore, the significantly enhanced n and simultaneously increased μ contribute to the improvement of σ of Te-doped SnSe materials.

Fig. 3d presents the variation of Seebeck coefficient α with the temperature. The values of α for all samples are positive over the entire temperature range, indicating the p-type electrical transport nature. With increasing temperature, the α increases firstly and then decreases at around 700 K, which should be attributed to the bipolar transport since noticeable minor charge carriers would be excited at high temperature [11,31]. It is shown that α reduces with the increasing Te concentration and all Te-doped samples have lower α values than that of undoped SnSe. Specifically, the maximum α decreases from 409 μV/K in the pristine SnSe to 339 μV/K in the $SnSe_{0.8}Te_{0.2}$. The reduction of α value with an increasing Te concentration is caused by the enhanced n [19,31].

The temperature-dependent power factor ($PF = \alpha^2\sigma$) is shown in Fig. 4a. The maximum PF value of 4.59 μW cm^{-1} K^{-2} is obtained at

Table 1
Lorenz number, Hall coefficient, volume density and relative density of bulk $SnSe_{1-x}Te_x$ samples at room temperature.

Sample	Lorenz number (10^{-8} V^2/K^2)	Hall coefficient (10^{-7} m^3/C)	Volume density (g/cm^3)	Relative density (%)
SnSe	1.504	6.414	6.08	98.38
$SnSe_{0.95}Te_{0.05}$	1.607	3.353	6.12	98.78
$SnSe_{0.90}Te_{0.10}$	1.647	2.453	6.17	99.35
$SnSe_{0.85}Te_{0.15}$	1.668	1.951	6.21	99.75
$SnSe_{0.80}Te_{0.20}$	1.652	1.847	6.22	99.67

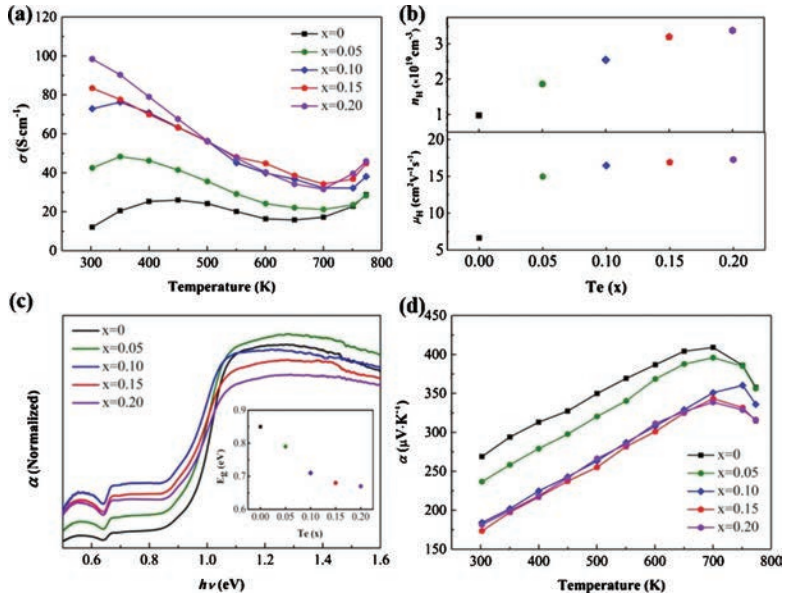

Fig. 3. (a) Temperature-dependent electrical conductivity of bulk $SnSe_{1-x}Te_x$. (b) Hall carrier concentration and mobility at 300 K. (c) Optical absorption spectra of $SnSe_{1-x}Te_x$. The inset shows the calculated optical band gap. (d) Temperature-dependent Seebeck coefficient.

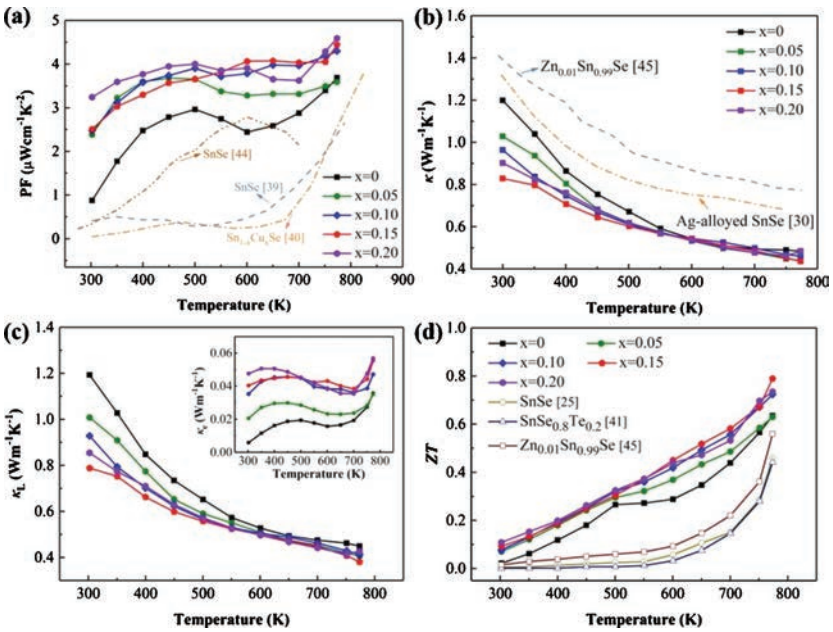

Fig. 4. Temperature dependence of (a) power factor, (b) total thermal conductivity, (c) lattice thermal conductivity with the inset showing the electronic thermal conductivity, and (d) *ZT* for bulk $SnSe_{1-x}Te_x$ samples together with the *ZT* data of some reported SnSe-based samples for comparison.

773 K in the $SnSe_{0.8}Te_{0.2}$ sample, which is higher than that of several previously reported polycrystalline SnSe [38,39,43]. Fig. 4b is the plots of total thermal conductivity κ as a function of the temperature. Generally, κ exhibits a decreasing trend with the rising temperature, suggesting enhanced phonon-phonon Umklapp scattering. All Te-doped samples show lower κ than that of reported Ag-doped SnSe [30] and Zn-doped polycrystalline SnSe [44]. Moreover, thetotal thermal conductivity of $0.79\ W\ m^{-1}\ K^{-1}$ has been observed at 300 K in the sample $SnSe_{0.85}Te_{0.15}$, showing a nearly 34% reduction in comparison to the undoped polycrystalline SnSe. It is well documented that κ value is mainly comprised of two terms, the electrical contribution (κ_e) and lattice contribution (κ_L), associated with the electrons and phonons, respectively. The κ_e can be estimated based on the Wiedemann–Franz law $\kappa_e = L\sigma T$ with L representing the Lorentz number, which could bederived from the single parabolic band model as following [30,45]:

$$L = \left(\frac{k_B}{e}\right)^2 \left[\frac{3F_2(\eta)}{F_0(\eta)} - \left(\frac{2F_2(\eta)}{F_0(\eta)}\right)^2\right]$$

where k_B and η are the Boltzmann constant and reduced Fermi level, respectively. η could be calculated using the measured Seebeck coefficient based on the following equation:

$$S = \frac{k_B}{e}\left[\frac{2F_1(\eta)}{F_0(\eta)} - \eta\right]$$

In the above equations, $F_n(\eta)$ is the generalized Fermi integration and given by:

$$F_n(\eta) = \int_0^\infty \frac{\varepsilon^n}{1+\exp(\varepsilon-\eta)}d\varepsilon$$

where ε is the reduced energy. In this work, the obtained L values for different $SnSe_{1-x}Te_x$ samples fluctuate around $\sim 1.6 \times 10^{-8}\,V^2/K^2$ (Table 1), which are in accordance with the reported value for SnSe [46]. Subtracting κ_e from κ, we calculated κ_L and shown the results in Fig. 4c. The small difference between κ and κ_L reveals that the heat transport of our $SnSe_{1-x}Te_x$ materials is mainly dominated by the phonon. It can be seen that κ_L reduces as Te doping content increases, which is due to the enhanced phonon scattering caused by point defect. Nevertheless, the lowest κ_L is obtained in the $SnSe_{0.85}Te_{0.15}$ sample rather than in the $SnSe_{0.8}Te_{0.2}$ sample. Owing to the similar grain size in all $SnSe_{1-x}Te_x$ samples, the strength of grain boundary scattering can be considered relatively identical among these samples. Therefore, the difference of κ_L with different Te doping content could be attributed to the synergistic effect of point defect scattering and Umklapp phonon scattering. Increasing Te doping level can not only strengthen the point defect scattering, but also affect the Umklapp scattering. According to previous study [22], the strong Umklapp scattering in SnSe is due to the strong anharmonicity of lattice dynamics resulting from the bonding instability. Such bond instability is driven by the resonantlybonding Se p-states, coupled to stereochemically active Sn lone pair. Substituting Te atoms into the Se site can change the bonding instability, giving rise to the weakened anharmonicity and thus diminishing Umklapp scattering in the $SnSe_{1-x}Te_x$ samples. On the whole, the opposite change trend of point defect scattering and Umklapp phonon scattering with increasing Te doping level gives rise to the lowest κ_L in the $SnSe_{0.85}Te_{0.15}$.

The ZT values of all $SnSe_{1-x}Te_x$ samples were calculated and presented in Fig. 4d. It can be seen that ZT increases with rising temperature and is improved in the whole temperature range by doping with Te. The ZT of $SnSe_{0.85}Te_{0.15}$ sample reaches a maximum value of 0.79 at a comparatively low temperature of 773 K, which is higher than that of previously reported polycrystalline SnSe materials at the same temperature [25,40,44]. This reveals that Te doping *via* hydrothermal approach is an effective route to enhance the thermoelectric performance of SnSe.

In summary, we have succeeded in fabricating p-type $SnSe_{1-x}Te_x$ polycrystalline nano-powders using eco-friendly and cost-effective hydrothermal approach and densifying the nano-powders by spark plasms sintering. The electrical conductivity for Te-doped bulk SnSe samples are greatly improved in the temperature range of 300–773 K, which is ascribed to the enhanced carrier concentration and mobility due to the band gap shrinking. As a result, an enhanced power factor is achieved in spite of the decreased Seebeck coefficient. On the other hand, the thermal conductivity at room temperature is significantly reduced from $1.20\,W\,m^{-1}\,K^{-1}$ for pristine SnSe to $0.79\,W\,m^{-1}\,K^{-1}$ for $SnSe_{0.85}Te_{0.15}$ sample, resulting from the strengthened point-defect scattering on phonon caused by doping Te on Se site. The simultaneous optimization of both power factor andthermal conductivitycontributes to a high ZT value of 0.79 at 773 K in $SnSe_{0.85}Te_{0.15}$. This work provides a facile and low-cost method to the mass production of polycrystalline SnSe with high thermoelectric performance for practical applications.

Declaration of competing interest

The authors declare that they have no known competing financial interests or personal relationships that could have appeared to influence the work reported in this paper.

Acknowledgements

This work was funded by the Fundamental Research Funds for the Central Universities (No. 2232020A-02), National Natural Science Foundation of China (Nos. 51774096, 51871053, 51902333), Shanghai Committee of Science and Technology (No. 18JC1411200), Program for Innovative Research Team in University of Ministry of Education of China (No. IRT_16R13). Q. Zhang acknowledges financial support sponsored by Shanghai Sailing Program (No. 19YF1454000) and Key Research Program of Frontier Sciences, CAS (No. ZDBS-LY-JSC037).

Appendix A. Supplementary data

Supplementary material related to this article can be found, in the online version, at doi:https://doi.org/10.1016/j.cclet.2020.04.046.

References

[1] K. Biswas, J.Q. He, I.D. Blum, et al., Nature 489 (2012) 414–418.
[2] X.Y. Zhou, Y.C. Yan, X. Lu, et al., Mater. Today 21 (2018) 974–988.
[3] G.J. Snyder, E.S. Toberer, Nat. Mater. 7 (2008) 105–114.
[4] Y.Z. Pei, X.Y. Shi, A. LaLonde, et al., Nature 473 (2011) 66–69.
[5] K.L. Peng, B. Zhang, H. Wu, et al., Mater. Today 21 (2018) 501–507.
[6] J.P. Heremans, V. Jovovic, E.S. Toberer, et al., Science 321 (2008) 554–557.
[7] Q.Y. Zhang, H. Wang, W.S. Liu, et al., Energy Environ. Sci. 5 (2012) 5246–5251.
[8] J.P. Heremans, C.M. Thrush, D.T. Morelli, Phys. Rev. B Condens. Matter Mater. Phys. 70 (2004) 115334.
[9] B.R. Ortiz, H. Peng, A. Lopez, et al., Phys. Chem. Chem. Phys. 17 (2015) 19410–19423.
[10] L.P. Hu, T.J. Zhu, X.H. Liu, et al., Adv. Funct. Mater. 24 (2014) 5211–5218.
[11] G.D. Tang, W. Wei, J. Zhang, et al., J. Am. Chem. Soc. 138 (2016) 13647–13654.
[12] D. Li, J.C. Li, X.Y. Qin, et al., Energy 116 (2016) 861–866.
[13] P. Jood, M. Ohta, Materials 8 (2015) 1124–1149.
[14] S. Bhattacharya, A. Bohra, R. Basu, et al., J. Mater. Chem. A 2 (2014) 17122–17129.
[15] D. Wu, L.D. Zhao, X. Tong, et al., Energy Environ. Sci. 8 (2015) 2056–2068.
[16] J.Q. He, J.R. Sootsman, S.N. Girard, et al., J. Am. Chem. Soc. 132 (2010) 8669–8675.
[17] Z.Z. Jian, Z.W. Chen, W. Li, et al., J. Mater. Chem. C 3 (2015) 12410–12417.
[18] A.T. Duong, V.Q. Nguyen, G. Duvjir, et al., Nat. Commun. 7 (2016) 13713.
[19] W. Wei, C. Chang, T. Yang, et al., J. Am. Chem. Soc. 140 (2018) 499–505.
[20] S.R. Popuri, M. Pollet, R. Decourt, et al., J. Mater. Chem. C 4 (2016) 1685–1691.
[21] F. Chu, Q.H. Zhang, Z.X. Zhou, et al., J. Alloys. Compd. 741 (2018) 756–764.
[22] L.D. Zhao, S.H. Lo, Y.S. Zhang, et al., Nature 508 (2014) 373–377.
[23] L.D. Zhao, C. Chang, G.J. Tan, et al., Energy Environ. Sci. 9 (2016) 3044–3060.
[24] Z.G. Chen, X.L. Shi, L.D. Zhao, et al., Prog. Mater. Sci. 97 (2018) 283–346.
[25] S. Sassi, C. Candolfi, J.B. Vaney, et al., Appl. Phys. Lett. 104 (2014) 212105.
[26] E.K. Chere, Q. Zhang, K. Dahal, et al., J. Mater. Chem. A 4 (2016) 1848–1854.
[27] N.K. Singh, S. Bathula, B. Gahtori, et al., J. Alloys. Compd. 668 (2016) 152–158.
[28] X. Lu, Q. Zheng, S. Gu, et al., Chin. Chem. Lett. 31 (2020) 880–884.
[29] Y.R. Gong, C. Chang, W. Wei, et al., Scr. Mater. 147 (2018) 74–78.
[30] C.L. Chen, H. Wang, Y.Y. Chen, et al., J. Mater. Chem. A 2 (2014) 11171–11176.
[31] T.R. Wei, G.J. Tan, X.M. Zhang, et al., J. Am. Chem. Soc. 138 (2016) 8875–8882.
[32] S. Chen, K.F. Cai, W.Y. Zhao, Physica B 407 (2012) 4154–4159.
[33] Z.H. Ge, K. Wei, H. Lewis, et al., J. Solid State Chem. 225 (2015) 354–358.
[34] D. Feng, Z.H. Ge, Y.X. Chen, et al., Nanotechnology 28 (2017) 455707.
[35] K.L. Peng, X. Lu, H. Zhan, et al., Energy Environ. Sci. 9 (2016) 454–460.
[36] Y.W. Li, F. Li, J.F. Dong, et al., J. Mater. Chem. C 4 (2016) 2047–2055.
[37] D. Feng, Z.H. Ge, D. Wu, et al., Phys. Chem. Chem. Phys. 18 (2016) 31821–31827.
[38] Y.L. Li, X. Shi, D.D. Ren, et al., Energies 8 (2015) 6275–6285.
[39] J.L. Gao, G.Y. Xu, Intermetallics 89 (2017) 40–45.
[40] T.R. Wei, C.F. Wu, X.Z. Zhang, et al., Phys. Chem. Chem. Phys. 17 (2015) 30102–30109.
[41] M. Hong, Z.G. Chen, L. Yang, et al., J. Mater. Chem. A 5 (2017) 10713–10721.
[42] J. Cho, M. Siyar, W.C. Jin, et al., Materials 12 (2019) 3854.
[43] W.H. Chen, Z.R. Yang, F.H. Lin, et al., J. Mater. Sci. 52 (2017) 9728–9738.
[44] J.C. Li, D. Li, X.Y. Qin, et al., Scr. Mater. 126 (2017) 6–10.
[45] Y.Z. Pei, Z.M. Gibbs, A. Gloskovskii, et al., Adv. Energy Mater. 4 (2014) 1400486.
[46] L.D. Zhao, G.J. Tan, S.Q. Hao, et al., Science 351 (2016) 141–144.